

GT2011-46753

SECONDARY FLOW STRUCTURES AND LOSSES IN A RADIAL TURBINE NOZZLE

Christoph K. Natkaniec, Jasper Kammeyer, and Joerg R. Seume

Institute of Turbomachinery and Fluid Dynamics
Leibniz Universität Hannover
Appelstrasse 9
DE-30167 Hannover, Germany
E-Mail: natkaniec@tfd.uni-hannover.de

ABSTRACT

An analysis of secondary flow structures and losses in a variable-vane radial turbine geometry is provided based on CFD. A complete turbine stage of a commercial vehicle turbocharger is modeled, including the entire 360° rotor and stator, in order to account for the circumferential non-uniformity of the flow. The full-stage model consists of approximately 12,500,000 nodes. The stator domain accounts for the endwall clearance on the hub side of the nozzle vanes. As an additional feature typical for variable turbine geometries, cylindrical shaft seals at the stator vane axis at hub and shroud as well as four circumferentially equidistant spacers are modeled.

These geometrical details allow a more realistic simulation of the stator domain. In an analysis using fields of helicity and Q-Criterion, the present features are found to induce additional secondary vortices in the stator, in addition to the inflow and horse shoe vortices found by previous investigators.

A detailed analysis of the secondary flow structures in this realistic stator shows that the spacers contribute 33% to the overall stator losses.

INTRODUCTION

Radial turbines with variable turbine geometry are widely used in turbocharger applications, especially for automotive applications. The applications range from small passenger cars to heavy duty vehicles. In the past decades, several investigations were carried out to assess and minimize losses in radial turbines with stator nozzles. These investigations mainly concerned larger radial turbines than those used in commercial vehicle turbochargers.

Hashemi et al. [1] investigated the flow in a radial nozzle cascade using air and water test rigs, respectively. Secondary flow structures in the air cascade were observed employing an oil and graphite powder mixture. The resulting pictures illustrated clearly the formation of horse shoe type vortices at

the leading edge of the nozzle vanes. Passage vortices known from axial turbines could not be found.

Eroglu and Tabakoff [2] used a three component LDV system to obtain detailed experimental data of the flow field in radial turbine guide vanes. The investigated nozzle comprised of 18 cambered vanes with a chord length of 50 mm. The authors found an influence of the scroll geometry on the flow field through the vane passage.

Putra and Joos [3] and Putra [4] carried out experimental and numerical investigations of the flow through the stator vane passage of an industrial radial turbine. Laser-two-focus (L2F) measurements were conducted to validate the numerical results. While horse shoe vortices could be located, the passage vortex observed in axial turbines was not found. Instead an additional vortex was observed, referred to as inflow vortex. This vortex was attributed to the asymmetric scroll geometry.

Simpson et al. [5] carried out full-stage CFD calculations of a turbocharger radial turbine nozzle. Detailed secondary flow structures were successfully captured. Horse shoe vortices were resolved of the type commonly observed in axial turbomachinery. In addition two counter-rotating inflow vortices resulting from the upstream housing geometry were observed. These secondary flow structures were shown to combine and have a significant influence on the overall loss levels.

Improvements of design methods for higher efficiencies demand improved knowledge of the internal flow structures and loss mechanisms throughout the turbine stage. The aim of this investigation is to study the secondary flow structures and losses in a radial turbine nozzle with the typical geometrical features of a real variable geometry turbine. These present features are the cylindrical shaft seals and the spacers.

NOMENCLATURE

c	Absolute Velocity	$[m \cdot s^{-1}]$
H	Helicity	$[m \cdot s^{-2}]$
H_{rel}	Relative Helicity	$[-]$
κ	Isentropic Exponent	$[-]$
∇	Nabla Operator	$[-]$
$\vec{\Omega}$	Vorticity Vector	$[s^{-1}]$
$ \vec{\Omega} $	Magnitude of the Vorticity Vector	$[s^{-1}]$
Ω	Vorticity Tensor, asymmetric part of ∇u	$[s^{-1}]$
p	Pressure	$[-]$
Q	Q-Criterion	$[-]$
ρ	Density	$[kg \cdot m^{-3}]$
S	Strain Rate Tensor, symmetric part of ∇u	$[s^{-1}]$
\vec{u}	Velocity Vector	$[m \cdot s^{-1}]$
$ \vec{u} $	Magnitude of the Velocity Vector	$[m \cdot s^{-1}]$
ζ_{Loss}	Loss Coefficient	$[-]$
ζ_{Stator}	Stator Loss Coefficient	$[-]$

Subscripts

1	Nozzle Inlet Position
2	Nozzle Outlet Position
s	Static
t	Total

DESIGN, NUMERICAL MODEL AND VALIDATION

The investigated turbocharger consist of an asymmetric volute, a variable nozzle with 12 stator vanes, four spacers and a standard design rotor with 11 blades. The stator vanes and the spacers are distributed equidistantly on the circumference. Figure 1 depicts parts of the rotor and stator geometry. The vane angle of the variable nozzle was set to 50% opened. Specific for the investigated geometry compared to geometries presented in available literature are the spacers and the cylindrical shaft seals. The rotor inlet diameter is smaller than the 86 mm turbine presented by Simpson et al. [5]. The vane height of the variable nozzle is 9.2 mm and the endwall clearance modeled at nozzle hub side is about 1% of the nozzle height.

For initial validation of the numerical model, steady state simulations were performed using a complete turbine stage, including full rotor and stator, in order to account for the circumferential non-uniformity of the flow. The computational model comprised of the domains inlet duct, volute, stator, rotor and outlet duct. The meshes were generated using the commercial meshing software ANSYS ICEM CFD. The volute was meshed with unstructured tetrahedral elements and prismatic elements in near wall regions so as to achieve higher accuracy of boundary layer flow prediction. The mesh was refined in the tongue region and in the torus region towards the interface to the stator domain, respectively. The grid size was set to 210,000 nodes. For the stator domain a completely structured hexahedral mesh was created using H- and L-grid

topologies. An O-grid topology was adopted around the vanes, the cylindrical shaft seals and the spacers to minimize skew angles and to resolve the boundary layer. The stator geometry with the four spacers made a meshing of a 90°-segment necessary. Each segment comprised of around 880,000 nodes which led to a total grid size of proximately 3,520,000 nodes in the stator domain. The endwall clearance was modeled on the hub side to capture tip leakage flows. For the rotor mesh rotational periodicity was used to mesh one blade passage with completely structured hexahedral elements comprising of 300,000 elements per passage. An O-grid topology was used to minimize skew angles at rotor hub and trailing edges and to resolve the boundary layer. The tip clearance between rotor blades and shroud was modeled to capture tip leakage flows. The total rotor mesh consists of approximately 3,300,000 nodes. The domains inlet duct, diffuser and outlet duct with pipelike geometry were meshed using structured hexahedral elements. The grid sizes were approximately 150,000, 100,000 and 150,000, respectively. The total mesh size for the full-stage numerical model is approximately 7,400,000 nodes. In a grid study carried out prior to the steady state model validation the results obtained with this mesh density showed global and local mesh independence.

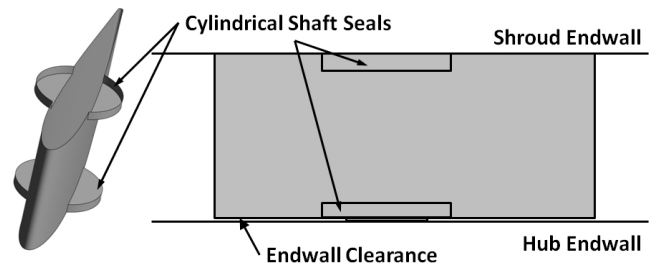
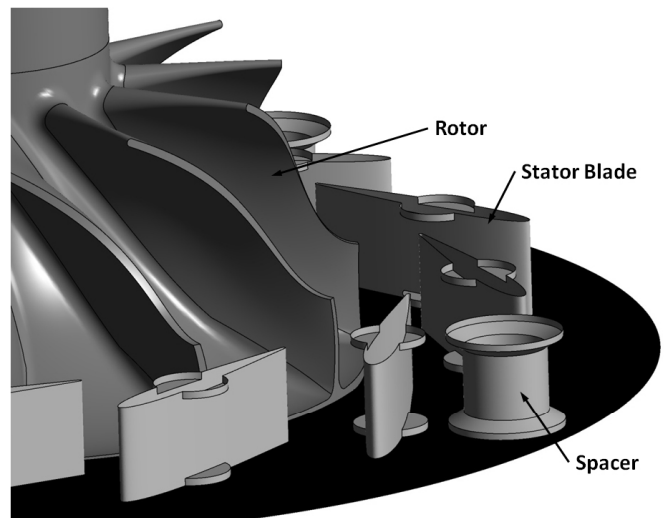


Figure 1: Geometric details of the variable nozzle

In order to obtain boundary conditions for the numerical simulations and for model validation purposes the turbocharger was measured on a hot gas test stand. Figure 2 illustrates the

turbocharger arrangement on the test stand. The full turbine map was measured. The test data comprises of total and static pressures and temperatures upstream and downstream of the turbine as well as mass flow rate.

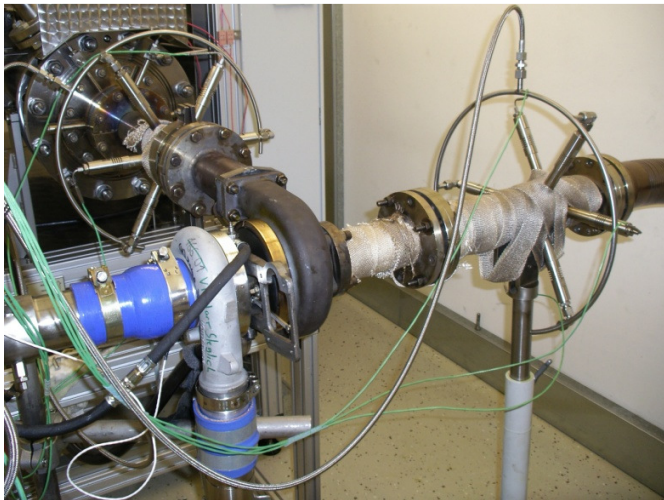


Figure 2: Experimental setup

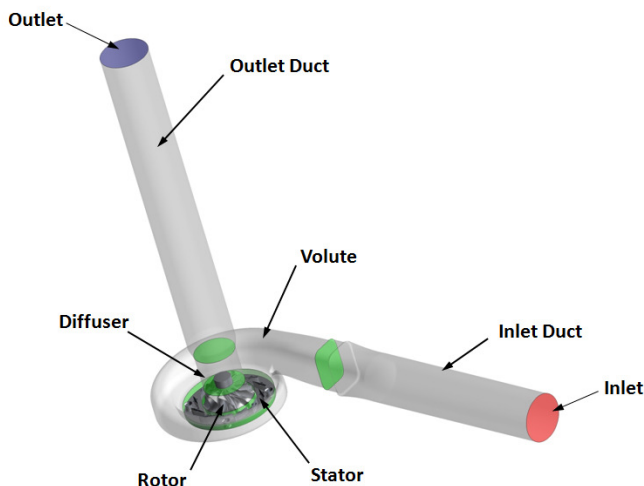


Figure 3: Full-stage numerical model

For the numerical simulations the commercial software ANSYS CFX was used. Figure 3 depicts the full-stage numerical model. The areas **Inlet** and **Outlet** marked red and blue, respectively, match with the positions of the pressure taps and thermocouples adopted at the test stand. The green surfaces indicate the interfaces between the different domains. As boundary conditions the mass flow rate and total temperature at the **Inlet**, the **Rotor** rotational speed and the static pressure at **Outlet** were set. For turbulence modeling the $k-\omega$ shear stress transport model (SST) was employed, as developed by Menter [6], [7]. Bardina et al. [8] compared the SST model with standard $k-\epsilon$ and $k-\omega$ models and found it to be superior in prediction of complex flows involving separation. The

connection of the stationary and rotating domains was modeled with the Frozen Rotor approach.

For the validation of the numerical model several operating points at different turbine rotational speeds obtained from the turbine map were calculated. Figure 4 displays a comparison of the experimental and numerical results in a typical turbine map. A quite good numerical map prediction is reached. Similar results for numerical turbine map prediction were presented by Suhrmann et al. [9].

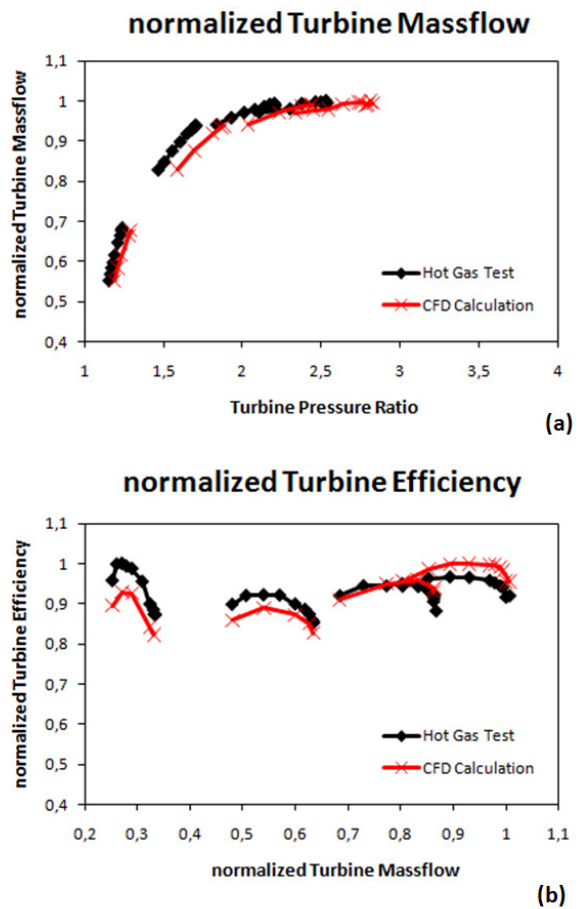


Figure 4: Comparison of experimental and numerical results, (a) normalized turbine mass flow, (b) normalized turbine efficiency

UNSTEADY MODELING

In order to resolve the secondary flow structures inside the variable nozzle an unsteady numerical simulation was carried out, subsequently. For this unsteady simulation the same full-stage model, as used in the steady state model validation, was adopted, c.f. Fig. 3. However, the mesh was refined to achieve an adequate spatial resolution of the computational domain for secondary flow investigation. A grid size of approximately 12,500,000 nodes for the complete full-stage model was created. The mesh size for the relevant stator

domain was almost doubled to approximately 6,400,000 nodes in total. To ensure accurately developed flow condition at stator inlet the resolution of the volute mesh was increased to approximately 900,000 nodes. The rotor mesh size, which was already highly resolved for the steady state simulation was put to approximately 4,400,000 nodes in total. The inlet duct, diffuser and outlet duct meshes were increased to approximately 380,000, 170,000 and 280,000, respectively. Initial results for the unsteady calculation were obtained from a converged steady state simulation computed prior to the unsteady calculation. For the interfaces of the stationary and rotating domains a sliding mesh interface was adopted. Using this approach the rotor is rotated by the corresponding angular displacement for each time step, with discrete calculations carried out at each position. As boundary conditions for the unsteady simulation a turbine pressure ratio of 2 at design speed was chosen. The time step was chosen to represent 0.2 degree of rotor rotation. The unsteady calculation was performed for three complete rotor rotations to ensure that convergence and consistency of the results were obtained. During the third rotor rotation, results were written for variables of interest for each one degree step. For turbulence modeling the k- ω SST turbulence model was adopted. Torre et al. [10] used a k- ω turbulence model to calculate secondary flows in a low pressure turbine. The authors found a significant level of agreement between the experimental data and the numerical results. They reported that the numerical results captured the secondary flow development.

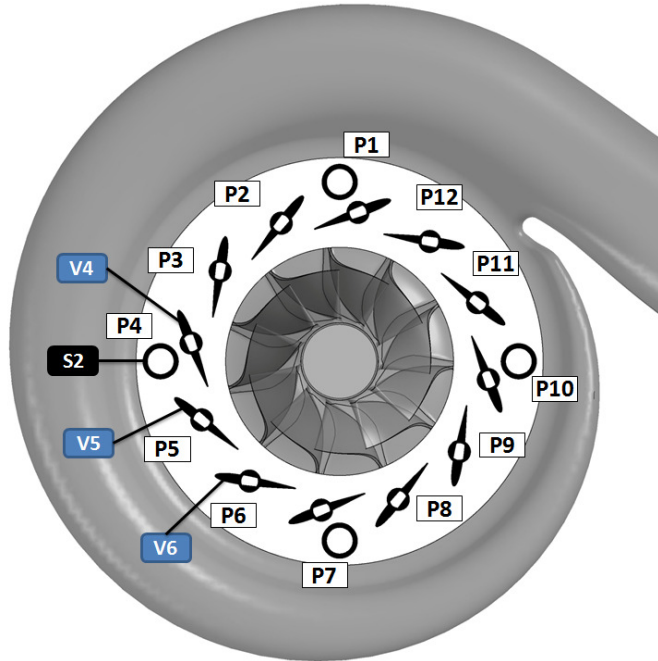


Figure 5: Overview of the variable nozzle

ANALYSIS OF THE SECONDARY FLOW STRUCTURES

For the secondary flow investigation the focus was put on the flow patterns in the region of the vanes V4, V5 and V6, spacer S2 and the passages P4, P5 and P6, as displayed in Fig. 5, which gives an overview of the variable nozzle and the regions of interest for secondary flow and loss inquiry. The region chosen for the secondary flow investigation was believed being located far away from the tongue, so that the flow structures would not be influenced by the tongue. The vane passages marked with P1 to P12 will be discussed later.

In order to localize and visualize the secondary flow structures inside the stator passages different methods suggested in the available literature were used.

The vorticity

$$\vec{\Omega} = \begin{pmatrix} \Omega_x \\ \Omega_y \\ \Omega_z \end{pmatrix} = \nabla \times \vec{u} \quad (1)$$

is the curl of the velocity vector \vec{u} . It indicates vortical structures.

For the localization and interpretation of secondary flows in turbomachinery Hawthorne [11], Lakshminarayana [12] and Gregory-Smith et al. [13] amongst other authors suggested the streamwise vorticity, which is also described as helicity by Torre et al. [10] and Anker et al. [14].

The helicity

$$H = \vec{\Omega} \cdot \vec{u} = (\nabla \times \vec{u}) \cdot \vec{u} \quad (2)$$

is the scalar product of the vorticity vector $\vec{\Omega}$ and the velocity vector in flow direction \vec{u} . The advantage of helicity over vorticity is that it identifies secondary flows more clearly. It indicates the sense of rotation of the secondary vortices and represents the rate of transport of secondary flow.

A qualitative approach to identify the sense of rotation of secondary vortices is the relative Helicity

$$H_{rel} = \frac{\vec{\Omega} \cdot \vec{u}}{|\vec{\Omega}| \cdot |\vec{u}|} = \frac{(\nabla \times \vec{u}) \cdot \vec{u}}{|\nabla \times \vec{u}| \cdot |\vec{u}|} \quad (3)$$

which is the helicity normalized by the product of the magnitudes of the vorticity vector $|\vec{\Omega}|$ and the velocity vector $|\vec{u}|$. While the helicity provides quantitative information about the secondary vortices, the relative helicity provides qualitative information of the location and sense of rotation of the secondary vortices. The color scale of the relative helicity in this investigation was set to blue and red ($-1 \leq blue < 0 < red \leq 1$) to indicate the sense of rotation of the secondary vortices. In streamwise direction blue identifies vortical structures with a counter clockwise sense of rotation, while red identifies vortical structures with a clockwise sense of rotation.

Another method to detect vortex core regions described by Green et al. [15] is the Q-Criterion

$$Q = \frac{1}{2}(\|\Omega\|^2 - \|S\|^2) > 0 \quad (4)$$

which was developed by Hunt et al. [16]. The Q-Criterion locates regions where rotation is dominant over strain in the flow, which is the case in vortex cores.

In the analysis detailed in this paper the Q-Criterion was employed at first to detect and visualize the vortex core regions inside the variable nozzle. Figure 6 illustrates the complexity of the vortical structures found with the Q-Criterion in the region of spacer S2. In order to identify the sense of rotation of the vortical structures found, the relative helicity was applied to the vortex core regions displayed by the Q-Criterion. This method allowed localizing and visualizing secondary vortices, but since the Q-Criterion is a method to detect vortex core regions in general it detects more than only secondary vortices. Consequently, the Q-Criterion is a necessary, but not sufficient criterion to identify secondary flow. Hence, another approach was necessary. For this reason surfaces perpendicular to a mean streamline in the vane passage were created. At these surfaces only the relative helicity was adopted. Figure 7 depicts the secondary flow patterns localized by sole relative helicity throughout the passage. The advantage of the relative helicity as applied in this investigation is that, it identifies the regions and displays the sense of rotation of secondary flows. The disadvantage is that, if there are several secondary vortices with the same sense of rotation in the same region it does not resolve the number of the secondary vortices in that region. For this reason the relative helicity is still not a sufficient criterion to localize all secondary flow structures. This can be solved by employing the helicity on the surfaces of interest.

Figure 6 and 7 give a good overview of the complexity of the secondary flows inside the variable nozzle. The authors decided to put the emphasis of the present investigation on the main secondary flow structures which are suspected to generate high losses. The focus was laid on the secondary flows caused by the cylindrical shaft seals and spacers. One goal was the derivation of schematic diagrams of the secondary vortices found at these geometric features.

To compare the influence of the spacers on secondary flow the investigation was conducted for the flow around vane V6 and passage P6 which are the least influenced regions by spacer S2. In order to capture the influence of spacer S2 on secondary flow structures the flow around vanes V4 and V5 and passage P4 was investigated. Figure 8 depicts the streamlines around the vanes V4, V5 and V6 as well as spacer S2. Furthermore, the location of interrogation surfaces is indicated. The direction of view on all interrogation surfaces is the streamwise direction.

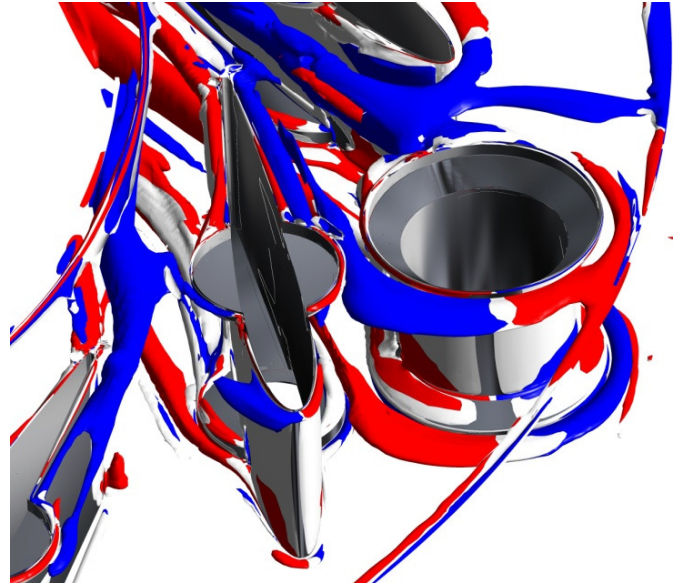


Figure 6: Highly complex vortex structures inside the variable nozzle – Visualized by Q-Criterion in combination with relative Helicity – View: Streamwise direction

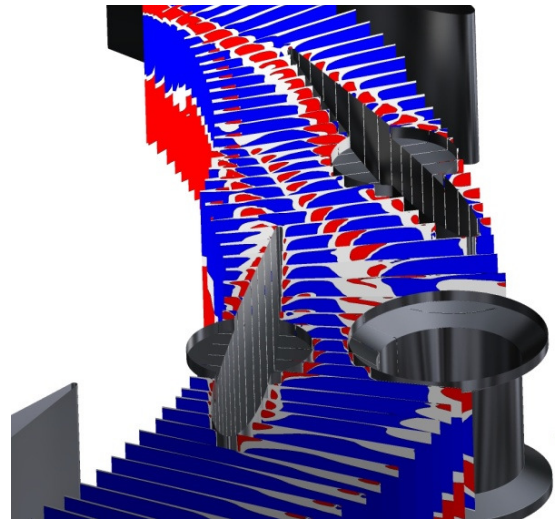


Figure 7: Surfaces through the spacer passage following a streamline to localize secondary vortices – Visualized by relative helicity – View: Streamwise direction

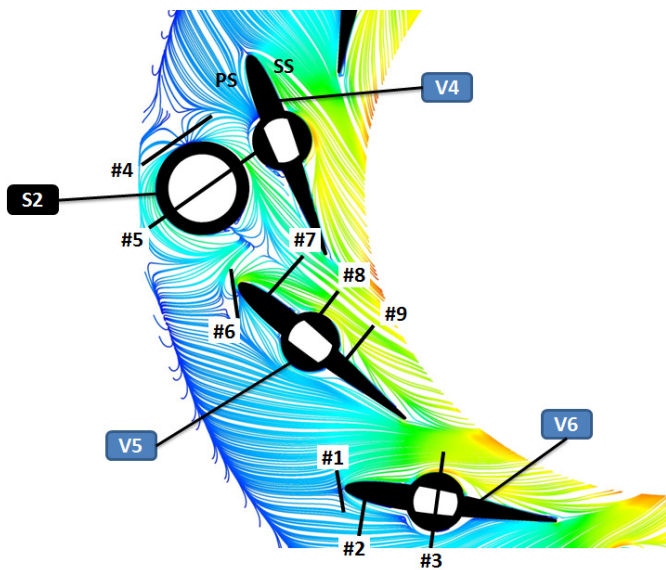


Figure 8: Streamlines at shroud side and location of the interrogation surfaces

For reasons of comparison with results presented by Putra and Joos [3] and Simpson et al. [5] and for validation, selected interrogation surfaces near or at vane V6 are displayed in Fig. 9, Fig. 10 and Fig. 11. The presence of horse shoe vortices formed at the vane leading edge and the presence of inflow vortices both described by Putra and Joos [3] and Simpson et al. [5] are confirmed. While horse shoe vortices are well known and documented from axial turbines, c.f. Sieverding [17], Langston [18] and Sharma et al. [19], the inflow vortices are specific to radial turbine nozzles. They are a direct product of the geometry upstream of the nozzle, as the entering flow from the volute is turned radially inward by the torus endwalls. The notation of vortices discussed in this paper is as follows. Inflow vortices, horse shoe and corner vortices are denoted IV, HSV and CV, respectively. Suction and pressure side of the vane or spacer are denoted with SS and PS, while hub and shroud are denoted with H and S, respectively. Figure 9 depicts the flow conditions in the form of helicity at surface 1 located at the leading edge of vane V6, indicating the formation of the suction and pressure side horse shoe vortices, denoted here with HSV SS and PS, respectively. Figure 10 (a) and (b) illustrates the flow conditions in the form of relative helicity and helicity superpositioned with secondary vectors at surface 2. Secondary vectors are defined as the velocity component of the flow vector perpendicular to the main flow direction. While the shroud side leg of the horse shoe vortex HSV PS S could be identified clearly in Fig. 10 (a) and (b), there is only a hint of the hub side leg of the horse shoe vortex HSV PS H. This can be attributed to the fact, that HSV PS H is being dragged inside the endwall clearance by the high momentum fluid passing the endwall clearance from pressure side to suction side.

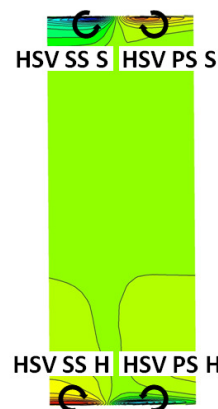


Figure 9: Helicity at surface 1

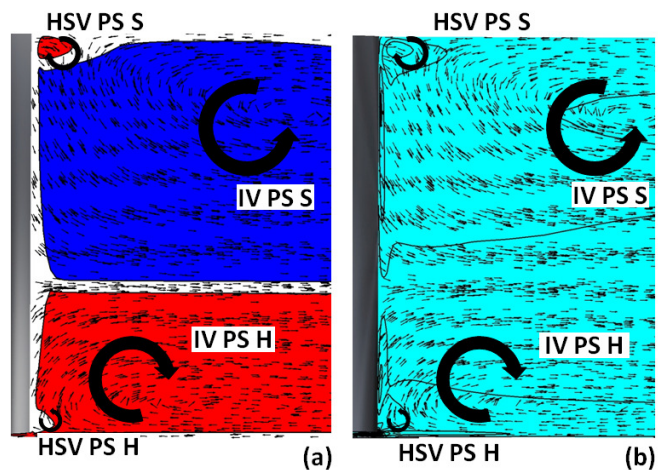


Figure 10: Relative helicity (a) and helicity (b) superpositioned with secondary vectors at surface 2

Moving further streamwise interesting secondary flow structures could be found at surface 3 depicted in Fig. 11. This surface displays a cross-section through the vane shaft axis. At the stagnation points of the cylindrical shaft seals near hub and shroud endwalls horse shoe vortices are formed, which propagate along the shaft seal wall indicated in Fig. 11 by HSV. As a consequence the inflow vortices (IV) are pushed from the hub and shroud endwalls inside the vane passage where they hit the vane surface with an obtuse angle leading to the formation of corner vortices (CV). The high momentum fluid of the inflow vortex drags the low momentum fluid in the corner between vane surface and shaft seal surface inducing a counter rotating corner vortex. Corner vortices are also well known from axial turbines, c.f. Lakshminarayana [12], Sieverding [17] and Langston [18]. To clarify the secondary flow structures around complex vane geometry, Fig. 12 illustrates a simplified schematic diagram of the secondary flow conditions at the cross-section of the vane shaft axis (surface 3) derived from the above mentioned observations.

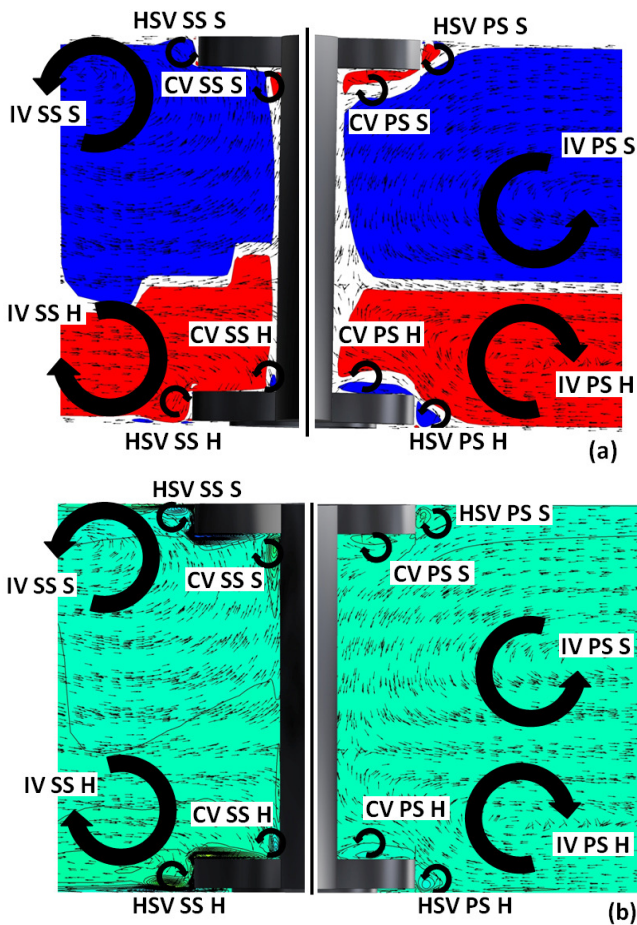


Figure 11: Relative helicity (a) and helicity (b) superpositioned with secondary vectors at surface 3

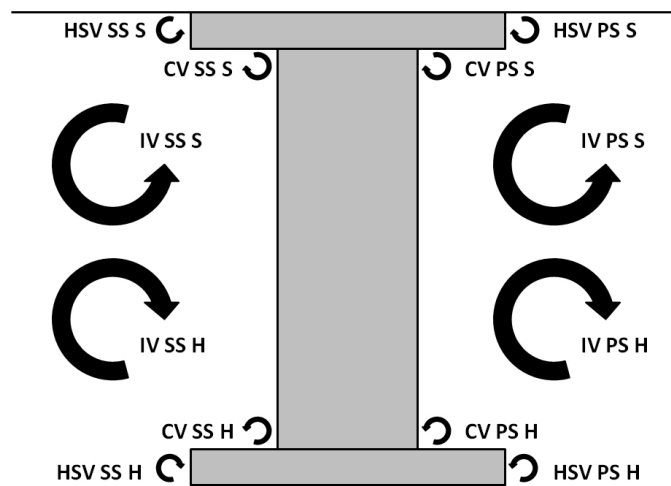


Figure 12: Schematic diagram of the secondary vortices around the vane at the cross-section of the vane shaft axis

For further inquiry the emphasis was put on helicity in order to achieve a higher resolution of the secondary vortices. Following the secondary flow structures induced by the spacer

are discussed. Figure 13 depicts the flow conditions in the form of helicity at surface 4 located at the stagnation point of spacer S2, indicating the formation of the pressure and suction side horse shoe vortices (HSV) and the inflow vortices (IV).

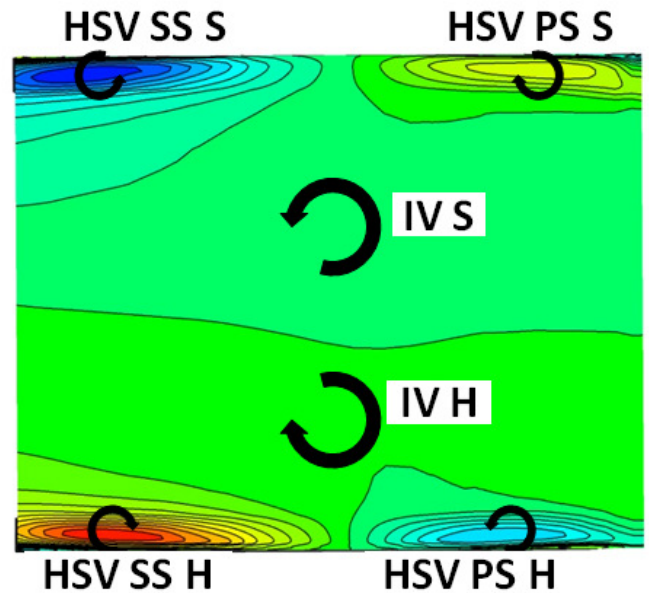


Figure 13: Helicity at surface 4

Following the streamwise direction along the spacer surface the propagation of the horse shoe vortices and the interaction between spacer S2 induced secondary vortices and vane V4 could be displayed at surface 5 in Fig. 14. The inflow vortices IV SS S and IV SS H are pushed inside the narrow passage between spacer S2 and vane V4 towards the surface of vane V4, inducing the corner vortices CV SS S V4 and CV SS H V4. While the horse shoe vortices HSV PS S and HSV PS H follow the spacer geometry, the horse shoe vortices HSV SS S and HSV SS H are being pushed away from the spacer surface due to separation.

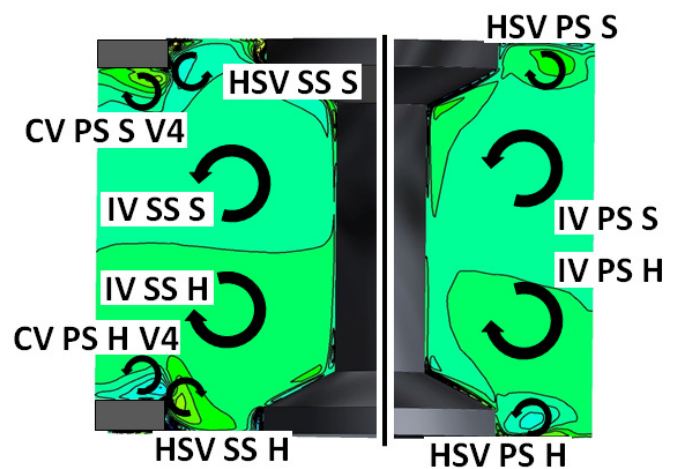


Figure 14: Helicity at surface 5

The two horse shoe vortices HSV SS S and HSV SS H induce corner vortices in the corner between the endwalls and the shaft seals. In the separation region where low momentum fluid is present the horse shoe vortices HSV SS S and HSV SS H drag the low momentum fluid and initiate counter rotating corner vortices. The latter mentioned formation of corner vortices was observed throughout the variable nozzle domain when high momentum secondary vortices trapped low momentum fluid between walls. Most of the smaller secondary vortices are dissipated by counter rotating or mixed with likewise rotating larger secondary vortices. From the observations of the flow around spacer S2 a general simplified schematic model displayed in Fig. 15 was derived similar to the one mentioned earlier, c.f. Fig. 12.

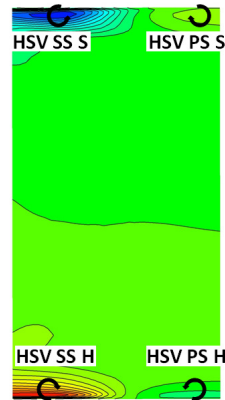


Figure 16: Helicity at surface 6

Additionally to the investigation of the secondary flow structures in the spacer S2 wake the local losses caused by the secondary vortices in this region were assessed using the loss coefficient

$$\zeta_{Loss} = \frac{\left(\frac{p_{t,1}}{p_t}\right)^{\frac{\kappa-1}{\kappa}} - 1}{\left(\frac{p_{t,1}}{p_s}\right)^{\frac{\kappa-1}{\kappa}} - 1} \quad (5)$$

suggested by Khalil et al. [20]. It describes the local total pressure loss relative to the total pressure at nozzle inlet.

In the spacer wake low momentum fluid is present. For this reason many secondary vortices are present, but primarily two can be identified as the main drivers of losses. These are the suction side horse shoe vortices HSV SS S V5 and HSV SS H V5 induced by the spacer S2 subsequent vane V5. Due to the pressure side incidence at the leading edge of vane V5 the fluid is accelerated towards the suction side, thus the horse shoe vortices HSV SS S V5 and HSV SS H V5 obtain a higher momentum. Entering the spacer S2 wake, where low momentum fluid is present, these vortices drag the low momentum fluid and grow, while propagating throughout the passage P4, displayed in Fig. 17, 18 and 19 for the surfaces 7, 8 and 9, respectively. The loss coefficients depicted in Fig. 17 (b), 18 (b) and 19 (b) show a good correlation with the vortex cores.

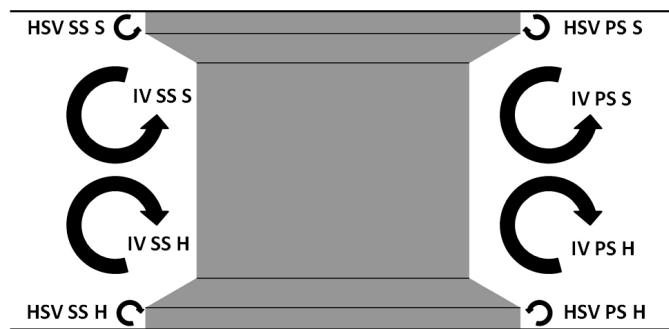


Figure 15: Schematic diagram of the secondary vortices around the spacer cross-section

For the further discussion of the secondary flow structures in the spacer S2 wake and the propagation of the secondary vortices throughout the passage P4 a look at the stagnation point of vane V5 must be taken. Figure 16 illustrates the flow conditions in the form of helicity at surface 6 located at the stagnation point of vane V5, indicating the formation of the pressure and suction side horse shoe vortices (HSV). Already at this point the suction side legs of the horse shoe vortices HSV SS S and HSV SS H are larger than the pressure side legs HSV PS S and HSV PS H. This can be explained from Fig. 8 by the strong pressure side incidence of vane V5, which is caused by the precedent spacer S2. The strong pressure side incidence leads to separation of the suction side horse shoe vortices HSV SS S and HSV SS H. The consequence is discussed below.

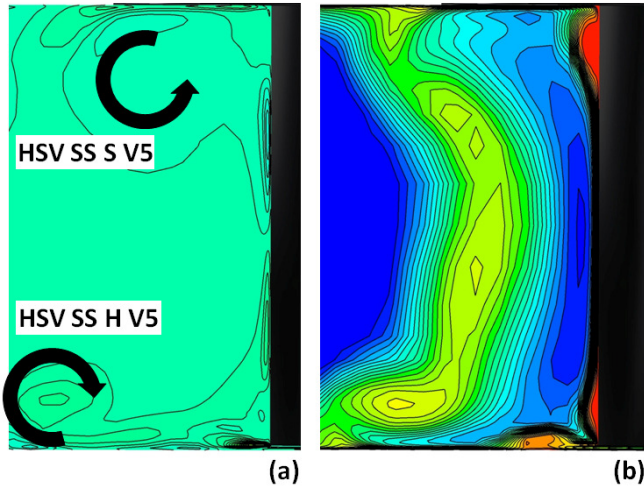


Figure 17: a) Helicity and b) loss coefficient at surface 7

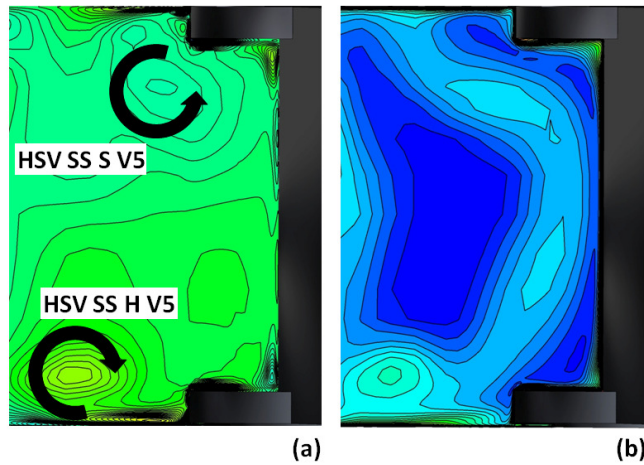


Figure 18: a) Helicity and b) loss coefficient at surface 8

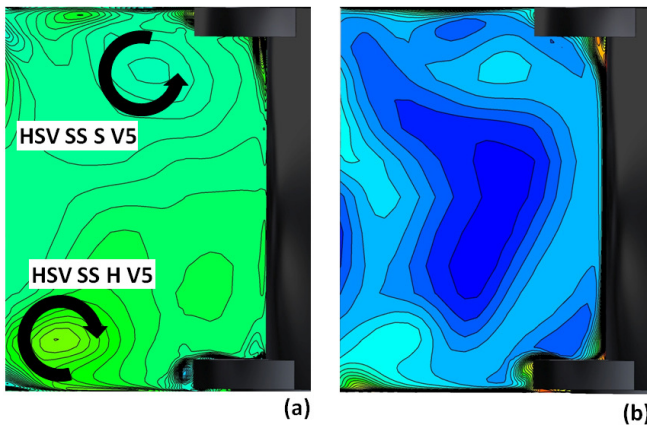


Figure 19: a) Helicity and b) loss coefficient at surface 9

ASSESSMENT OF THE LOSSES INSIDE THE VARIABLE NOZZLE

In order to achieve a global loss assessment on the influence of the spacers on the stator losses the stator loss coefficient

$$\zeta_{Stator} = \frac{p_{t,1} - p_{t,2}}{p_{t,2} - p_{s,2}} = \frac{p_{t,1} - p_{t,2}}{\frac{1}{2} \rho_2 c_2^2} \quad (6)$$

described by Denton [21] and Simpson et al. [5] was evaluated for each of the stator passages introduced in Fig. 5.

Additionally to the stator loss coefficient, the relative total pressure loss and the relative entropy rise were calculated for all 12 stator passages. The obtained results for total pressure and entropy were mass flow averaged. Furthermore, the relative mass flow rate was calculated for all 12 passages, as well. Figures 20 to 23 display the distributions for relative total pressure loss, stator loss coefficient, relative entropy rise and relative mass flow over the stator passages, respectively. The passages P1, P4, P7 and P10 are the passages, where the spacers are located. From figures 20 to 23 the influence of the spacers on the losses is obvious. Regarding, that passage P1 is located subsequently to the tongue, a contribution of the tongue on losses of passage P1 can be observed.

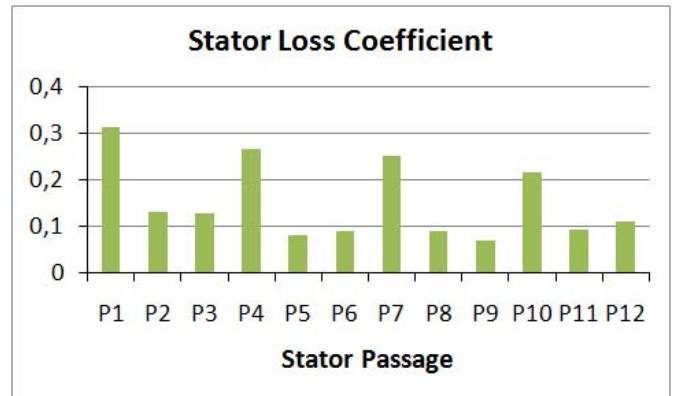


Figure 20: Stator loss coefficient

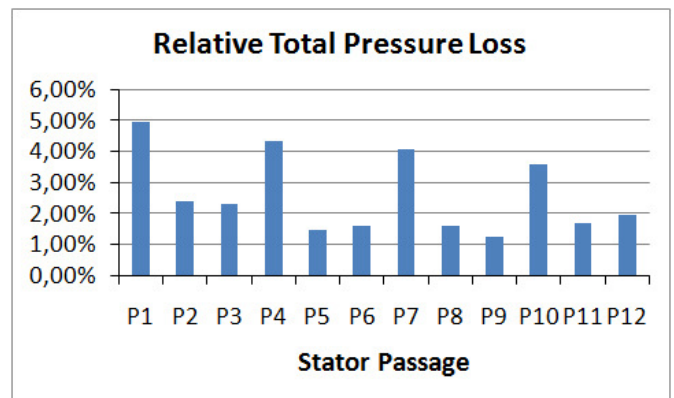


Figure 21: Relative total pressure loss

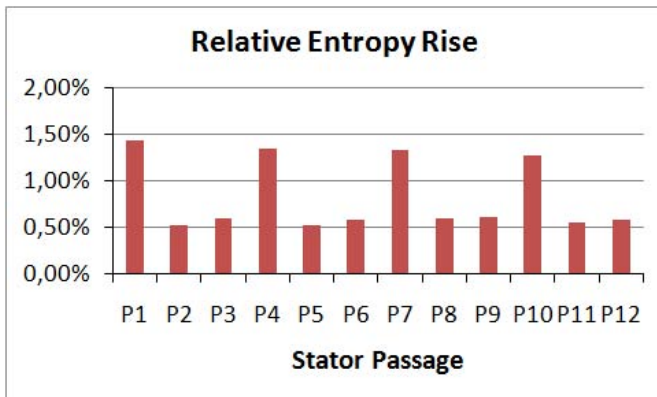


Figure 22: Relative entropy rise

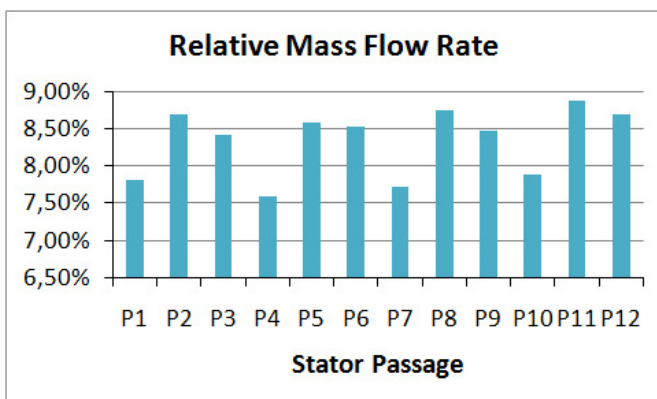


Figure 23: Relative mass flow rate

The upper results obtained from the global stator loss analysis can be explained by the local secondary flow losses induced in the wake of stator S2 displayed in Fig. 17 to 19. A correlation between the secondary flow losses due to spacers and the stator losses seems to be obvious.

Finally, the stator loss coefficient for the presented variable nozzle was calculated to be 14.8%. Assuming the same variable nozzle without spacers the stator loss coefficient would be reduced to 9.8%. Thus, the spacer induced stator losses were found to be 5% points in the present case. The spacers contribute 33% to the stator overall losses.

CONCLUSIONS

The influence of typical geometrical features on the secondary flow structures inside a variable turbine nozzle of a commercial vehicle turbocharger are investigated in a 360° full stage. Unsteady CFD simulation using a highly resolved mesh with 12,500,000 nodes is performed. High time resolution of 0.2 degree of rotor rotation is used. Three full rotor rotations are calculated to reach a periodic steady state.

At the cylindrical shaft seals at the stator vane hub and shroud ends, horse shoe vortices develop along the endwalls. In the area between the cylindrical shaft seals and the vane surface, corner vortices are induced by the two counter rotating inflow vortices, evolving through the stator passages. At the

four circumferentially equidistant spacers, horse shoe vortices at hub and shroud endwalls are found. The low momentum fluid in the wakes of the spacer allows the suction side horse shoe vortices on the next stator vane (following the spacer in the direction of rotation) to grow and propagate through the stator passages causing additional losses.

The losses induced by the spacers are quantified: The stator loss coefficient for the stator passages with spacers is more than twice as high as the stator loss coefficient for stator passages without spacers. Spacers do not only cause higher losses in the upstream passage, but also disturb the flow in the preceding and the subsequent stator vane passages. The spacers were found to contribute 33% to the stator overall losses.

Regarding the secondary flow structures inside a radial turbine stator nozzle, this investigation shows corner vortices at the shaft seals and horse shoe vortices from the spacers, in addition to the previously found inflow vortices and horse shoe vortices from the vane leading edge.

Further investigation will be carried out to separate the influence of the shaft seals, spacers, and endwall clearance on the stator losses in order to enhance the understanding of the loss behavior of the single geometrical features.

The propagation of the secondary flow patterns as well as the propagation of the losses into the rotor passages will be subject to further investigation. The influence of the loss propagation on turbine performance will be determined.

The secondary flow patterns propagating to the rotor also cause pressure differences on the pressure and suction side of the rotor blade. These pressure differences lead to excitation of the turbine wheel, which increases the risk of high cycle fatigue (HCF) failure, as reported by Heuer et al. [22]. The highly resolved unsteady CFD calculations presented in this paper represent a promising approach to determine the complex mechanisms of turbine excitation due to secondary flow in the variable nozzle.

Based on the presented and future investigations general design guidelines for variable nozzle turbines should be derived.

ACKNOWLEDGMENTS

The authors would like to acknowledge the technical and hardware support of Voith Turbo Aufladungssysteme GmbH, without which this investigation would not have been possible. Thanks are also due to Mr. Henning Scheel for his contribution to this project. The authors also acknowledge the contribution of the North-German Supercomputing Alliance (HLRN) with the computing power provided.

REFERENCES

- [1] Hashemi, S. G. R.; Lemak, R. J.; Owczarek, J. A.: An Investigation of the Flow Characteristics and of Losses in Radial Nozzle Cascades. ASME Journal of Engineering for Gas Turbines and Power, Vol. 106, pp. 502-510, 1984
- [2] Eroglu, H.; Tabakoff, W.: LDV measurements and investigation of flow field through radial turbine guide

- vanes. *ASME Journal of Fluids Engineering*, Vol. 113, No. 4, pp. 660-667, 1991
- [3] Putra, M. A.; Joos, F.: Investigation of secondary flow behavior in a radial turbine nozzle. Proceedings of the ASME Turbo Expo, Barcelona, Spain, 2006
- [4] Putra, M. A.: Untersuchungen zur Sekundärströmung eines radialen Turbinengitters. Dissertation Helmut-Schmidt-Universität, Universität der Bundeswehr Hamburg, 2005
- [5] Simpson, A. T.; Spence, S. W. T.; Watterson, J. K.: A Comparison of the Flow Structures and Losses Within Vaned and Vaneless Stators for Radial Turbines. *ASME Journal of Turbomachinery*, Vol. 131, No. 3, pp. 1-15, 2009
- [6] Menter, F. R.: Zonal two equation k-w turbulence models for aerodynamic flows. AIAA Fluid Dynamics Conference, 24th, 6-9 Jul., Orlando, United States, 1993
- [7] Menter, F. R.: Two-equation eddy-viscosity turbulence models for engineering applications. *AIAA Journal*, Vol. 32, No. 8, pp. 1598-1605, 1994
- [8] Bardina, J. E.; Huang, P. G.; Coakley, T. J.: Turbulence Modeling Validation, Testing and Development. NASA Technical Memorandum 110446, 1997
- [9] Suhrmann, J. F.; Peitsch, D.; Gugau, M.; Heuer, T.; Tomm, U.: Validation and Development of Loss Models for Small Size Radial Turbines. Proceedings of the ASME Turbo Expo, Glasgow, UK, 2010
- [10] Torre, D.; Vázquez, R., de la Rosa Blanco, E.; Hodson, H. P.: A New Alternative for Reduction in Secondary Flows in Low Pressure Turbines. *ASME Journal of Turbomachinery*, Vol. 133, No. 1, pp. 1-10, 2011
- [11] Hawthorne, W. R.: Rotational Flow Through Cascades. *Journal of Mechanics and Applied Mathematics*, Vol. 3, pp. 266-279, 1955
- [12] Lakshminarayana, B.: Fluid Dynamics and Heat Transfer of Turbomachinery. John Wiley & Sons, Inc., New York, 1996
- [13] Gregory-Smith, D. G.; Graves, C. P.; Walsh, J. A.: Growth of Secondary Losses and Vorticity in an Axial Turbine Cascade. *ASME Journal of Turbomachinery* 110, No. 1, pp. 1-8, 1988
- [14] Anker, J. E.; Mayer, J. F.; Casey, M. V.: The Impact of Rotor Labyrinth Seal Leakage Flow on the Loss Generation in an Axial Turbine. Proceedings of the Institution of Mechanical Engineers, Part A: Journal of Power and Energy, Vol. 219, pp. 481-490, 2005
- [15] Green, M. A.; Rowley, C. W.; Haller, G.: Detection of Lagrangian coherent structures in three-dimensional turbulence. *Journal of Fluid Mechanics*, Vol. 572, pp. 111-120, 2007
- [16] Hunt, J. C. R.; Wary, A. A.; Moin, P.: Eddies, Streams, and Convergence Zones in Turbulent Flows. Proceedings of the Summer Program of the Center for Turbulent Research, pp. 193-207, 1988
- [17] Sieverding, C. H.: Recent Progress in the Understanding of Basic Aspects of Secondary Flows in Turbine Blade Passages. *ASME Journal of Engineering for Gas Turbines and Power*, Vol. 107, No. 2, pp. 248-257, 1985
- [18] Langston, L. S.: Secondary Flow in Axial Turbines. *Annals of the New York Academy of Sciences, Heat Transfer in Gas Turbine Systems*, Vol. 934, pp. 11-26, 2001
- [19] Sharma, O. P.; Butler, T. L.: Predictions of Endwall Losses and Secondary Flows in Axial Flow Turbine Cascades. *ASME Journal of Turbomachinery*, Vol. 109, No. 2, pp. 229-236, 1987
- [20] Khalil, I. M.; Tabakoff, W.; Hamed, A.: Losses in Radial Inflow Turbines. *ASME Journal of Fluids Engineering*, Vol. 64, pp. 364-373, 1976
- [21] Denton, J. D.: Loss Mechanisms in Turbomachines. *ASME Journal of Turbomachinery*, Vol. 115, No. 4, pp. 621-656, 1993
- [22] Heuer, T.; Gugau, M.; Klein, A.; Ansel, P.: An Analytical Approach to Support High Cycle Fatigue Validation for Turbocharger Turbine Stages. Proceedings of the ASME Turbo Expo, Berlin, Germany, 2008